Title
Multidimensional MR spectroscopic imaging of prostate cancer in vivo.

Journal
NMR in biomedicine, 27(1)

ISSN
0952-3480

Authors
Thomas, M Albert
Nagarajan, Rajakumar
Huda, Amir
et al.

Publication Date
2014

DOI
10.1002/nbm.2991

Peer reviewed

Special issue review article

NMR IN BIOMEDICINE

Received: 28 January 2013, Revised: 12 April 2013, Accepted: 21 May 2013, Published online in Wiley Online Library: 31 July 2013

(wileyonlinelibrary.com) DOI: 10.1002/nbm.2991

Multidimensional MR spectroscopic imaging of prostate cancer *in vivo*

M. Albert Thomas[a]*, Rajakumar Nagarajan[a], Amir Huda[a,b], Daniel Margolis[a], Manoj K. Sarma[a], Ke Sheng[c], Robert E. Reiter[d] and Steven S. Raman[a]

Prostate cancer (PCa) is the second most common type of cancer among men in the United States. A major limitation in the management of PCa is an inability to distinguish, early on, cancers that will progress and become life threatening. One-dimensional (1D) proton (^{1}H) MRS of the prostate provides metabolic information such as levels of choline (Ch), creatine (Cr), citrate (Cit), and spermine (Spm) that can be used to detect and diagnose PCa. *Ex vivo* high-resolution magic angle spinning (HR-MAS) of PCa specimens has revealed detection of more metabolites such as myo-inositol (mI), glutamate (Glu), and glutamine (Gln). Due to the J-modulation and signal overlap, it is difficult to quantitate Spm and other resonances in the prostate clearly by single- and multivoxel-based 1D MR spectroscopy. This limitation can be minimized by adding at least one more spectral dimension by which resonances can be spread apart, thereby increasing the spectral dispersion. However, recording of multivoxel-based two-dimensional (2D) MRS such as J-resolved spectroscopy (JPRESS) and correlated spectroscopy (L-COSY) combined with 2D or three-dimensional (3D) magnetic resonance spectroscopic imaging (MRSI) using conventional phase-encoding can be prohibitively long to be included in a clinical protocol. To reduce the long acquisition time required for spatial encoding, the echo-planar spectroscopic imaging (EPSI) technique has been combined with correlated spectroscopy to give four-dimensional (4D) echo-planar correlated spectroscopic imaging (EP-COSI) as well as J-resolved spectroscopic imaging (EP-JRESI) and the multi-echo (ME) variants. Further acceleration can be achieved using non-uniform undersampling (NUS) and reconstruction using compressed sensing (CS). Earlier versions of 2D MRS, theory of 2D MRS, spectral apodization filters, newer developments and the potential role of multidimensional MRS in PCa detection and management will be reviewed here. Copyright © 2013 John Wiley & Sons, Ltd.

Keywords: prostate cancer; magnetic resonance spectroscopy; 2D JPRESS; 2D L-COSY; citrate; spermine; echo-planar spectroscopic imaging

INTRODUCTION

Prostate cancer (PCa) is the second leading cause of cancer deaths after lung cancer (1). The most common diagnostic tools used to look for evidence of PCa include digital rectal examination (DRE), serum concentration of prostate specific antigen (PSA) and transrectal ultrasonography (TRUS) guided prostate biopsy (2). The primary system for prognosis of PCa is based on the size and volume of cancer in a prostate biopsy specimen graded microscopically according to the glandular pattern of cancers (Gleason score, GS) (3). The GS is the sum of the two most common patterns (grades 1–5) of tumor growth found. In needle biopsy, it is now recommended that the worst grade should always be included even if present in less than 5% (4). Most PCa lesions are located in the peripheral zone (PZ) of the prostate and may be detected by DRE when the volume is about 0.2 ml or larger (5–7).

Digital rectal examination has a low overall sensitivity (37%) and low positive predictive value (PPV) when lower PSA levels

* *Correspondence to: M. A. Thomas, Department of Radiological Sciences, David Geffen School of Medicine, University of California, Los Angeles, CA 90095, USA. E-mail: athomas@mednet.ucla.edu*

a *M. A. Thomas, R. Nagarajan, A. Huda, D. Margolis, M. K. Sarma, S. S. Raman Department of Radiological Sciences, David Geffen School of Medicine, University of California, Los Angeles, CA 90095, USA*

b *A. Huda Department of Physics, California State University, Fresno, CA 93740, USA*

c *K. Sheng Department of Radiation Oncology, David Geffen School of Medicine, University of California, Los Angeles, CA, USA*

d *R. E. Reiter Department of Urology, David Geffen School of Medicine, University of California, Los Angeles, CA, USA*

Abbreviations used: *JPRESS, J-resolved spectroscopy; MRSI, magnetic resonance spectroscopic imaging; CS, compressed sensing; NUS, non-uniform undersampling; L-COSY, localized correlated spectroscopy; PCa, prostate cancer; BPH, benign prostatic hyperplasia; PZ, peripheral zone; PSA, prostate specific antigen; Ch, choline; Cr, creatine; Cit, citrate; Spm, spermine; Glu, glutamate; Gln, glutamine; Tau, taurine; GPC, glycerylphosphocholine; GSH, glutathione; TRUS, transrectal ultrasound; GS, Gleason score; CT, coherence transfer; T2W, T_2 weighted; DWI, diffusion-weighted imaging; ADC, apparent diffusion coefficient; MVD, microvessel density; DCE, dynamic contrast enhanced; 1D, one dimensional; 2D, two dimensional; 3D, three dimensional; 4D, four dimensional; SNR, signal to noise ratio; EPI, echo-planar imaging; EPSI, echo-planar spectroscopic imaging; SV, single volume; EP-COSI, echo-planar correlated spectroscopic imaging; EP-JRESI, echo-planar J-resolved spectroscopic imaging; ME, multi-echo; FFT, fast Fourier transform; ProFit, prior knowledge fitting; CRLB, Cramér–Rao lower bound.*

(0–3 ng /ml) are encountered (8). PSA measurement has yielded higher detection rates than DRE (7), but its specificity is low (36%) owing to false-positive PSA elevation under benign circumstances, such as inflammation or benign prostatic hyperplasia (BPH) (9). These inaccurate tools often lead to incorrect diagnoses, inaccurate risk assessments, patient anxiety, and less optimal therapy choices in management of the disease. Hence, there is a need for improved PCa diagnosis with better-detection, localization, and sampling. Prostate cancer is the only major solid organ malignancy that lacks an imaging-based diagnosis.

Diagnostic imaging methods currently in use, such as computerized tomography (CT) and ultrasound (US), cannot adequately detect PCa. MRI offers exquisite anatomical details, but may suffer from poor specificity in detecting and grading PCa (10,11). T_2-weighted (T2W) MRI delineates most larger foci of PCa as a region of low signal intensity surrounded by high signal intensity (longer T_2) of normal PZ tissue (12,13). Although the sensitivity of T2W images for tumor detection is high, specificity is suboptimal (14).

Low specificity may, however, lead to overtreatment, cause great anxiety to patients, and result in many unnecessary biopsies in patients with no or low grade cancers. On the other hand, if the patient with high grade cancer inappropriately chooses "active surveillance" as a management option, malignant cells can metastasize to the other parts of the body before the cancer becomes clinically evident. Thus more sensitive and specific non-invasive tests are needed to better differentiate indolent and aggressive PCa.

Techniques such diffusion-weighted imaging (DWI) and perfusion may improve the performance of MR. DWI is an MRI technique that visualizes molecular diffusion, that is, the Brownian motion of water molecules in biologic tissues (15), by applying two equally sized diffusion-sensitizing gradients, which are characterized by their *b*-values. The mobility is then quantified by calculating the apparent diffusion coefficient (ADC), which depends mainly on the cellularity, cell size, extracellular space, and temperature. When DWI is combined with T2W MRI, both sensitivity and specificity increase substantially. Sensitivity increases from a range of 49–88% for either modality alone to a range of 71–89% with the two modalities combined, while specificity increases from a range of 57–84% to a range of 61–91% (16–18).

Angiogenesis, the formation of new blood vessels, is often associated with malignancy (19,20). A number of studies have reported an increased microvessel density (MVD) in PCa, potentially enabling the detection or localization of tumors through imaging techniques sensitive to these characteristics (21–24). DCE-MRI of PCa is often found to enhance more quickly, to a greater degree, and to show more washout than the benign PZ (22,25–28). Malignant tissue differs from benign tissue with respect to microvessel density, blood flow, vascular morphology and permeability, and flow dynamics (29). A growing body of literature suggests that DCE-MRI may significantly improve cancer detection, tissue characterization, localization, and staging (30–33). According to a study by Kim *et al.*, DCE-MRI has been found to improve accuracy, sensitivity, and specificity by 26%, 31%, and 22% respectively relative to 1.5 T T2W imaging alone (34). Another study by the same group at 3 T also confirmed the superiority of DCE-MRI over T2W imaging (35). However, reports of correlation between DCE-MRI and specific tissue properties such as GS and MVD have been mixed, with both significant (24,36,37) and non-significant (26,38) findings. Moreover, mechanisms governing both qualitative and quantitative changes are not yet fully understood.

MR SPECTROSCOPIC IMAGING OF PROSTATE USING 1D SPECTROSCOPY

MRS is a non-invasive and powerful biochemical technique, which can be performed after the MRI protocol. Four metabolites, namely citrate (Cit), creatine (Cr), spermine (Spm), and choline (Ch) are the ones commonly detected in PCa (39,40). The resonances of the above mentioned metabolites occur at distinct frequencies (approximately 2.6 ppm, 3.03 ppm, 3.1 ppm, and 3.2 ppm, respectively). In healthy prostate tissues, Cit is secreted by the epithelial cells of the prostate in large amounts along with high levels of zinc, which inhibit the oxidation of Cit in the Krebs cycle. In the presence of cancer, the Cit level is dramatically diminished due to significant reduction of zinc in the cancerous epithelial tissue. Concurrently, the Ch level is elevated due to increased cell membrane turnover in the proliferating malignant tissues. Magnetic resonance spectroscopic imaging (MRSI) is promising as a valuable technique for evaluating the extent and aggressiveness of primary and recurrent PCa (10,11). Instead of single voxels, MRSI provides spectra from three-dimensional (3D) spatial arrays of contiguous volumes mapping the entire prostate. MRI and MRSI both are used for detailed anatomic and metabolic evaluations of the prostate. The (Ch + Cr)/Cit ratio is usually used as a criteria for the diagnosis of PCa in the 3D MRSI studies.

A major limitation of the MRSI using 1D spectra is its severe spectral overlap because of limited spectral dispersion at clinically used static magnetic field strengths ($B_0 \leq 3$ T). Low spectral dispersion causes a large number of metabolites to overlap within a small range of ^{1}H spectra (0–5 ppm) (41). Consequently, it makes quantification of metabolites very challenging. Further, water and lipid suppression using Mescher–Garwood (MEGA) RF pulses are combined with the localizing point resolved spectroscopy (PRESS) or stimulated echo acquisition mode (STEAM) sequence. This has resulted in a long TE-based MRSI acquisition since the 1990s (10,11,42). Spectral editing techniques (43–47) are generally optimized for detecting one specific metabolite, and hence may not be optimal for simultaneously detecting a large number of metabolites in clinical practice.

SINGLE VOXEL BASED 2D MR SPECTROSCOPY OF PROSTATE CANCER

Different versions of multidimensional techniques have been reported to overcome the signal overlap and to detect several metabolites more unambiguously than conventional MRSI techniques including spectral editing (46–56). Multidimensional MRS enables detection of a larger number of resonances from multiple metabolites with improved spectral resolution than one-dimensional (1D) MRS and a more efficient and accurate identification and quantification of metabolites. There are several books explaining various theoretical aspects of 2D MRS (57–59). Here, we present a brief theoretical explanation to describe the acquisition and post-processing of 2D MRS.

Theory

In the recording of single-voxel-based 1D spectroscopy, once the boundaries of the voxel are spatially localized with slice-selective RF pulses, differences in frequencies of ^{1}H for different metabolites are attributed to chemical shift or shielding

experienced by the proton in the particular electronic environment and indirect spin–spin coupling (J-coupling) communicated through covalent bonds. Chemical shift results in distribution of signal over several peaks originating from different magnetically non-equivalent proton groups. J-coupling splits the amplitude of each group further, and distributes it over multiplets arising from indirect coupling of magnetically non-equivalent protons mediated by electron–nuclear and electron–electron interactions. Overlap of these multiplets makes quantitation of different metabolites difficult.

2D L-COSY and JPRESS

The idea behind multidimensional spectroscopy is to pry open these interactions and observe their relationships in action. The sequences are designed to see how a spin group modifies its response when another is perturbed in some way. This brings to the foreground the correlation between interacting spin groups, which is the basis of correlated spectroscopy (COSY) (52,57). The three-dimensional (3D) spatially resolved analog of 2D COSY was named "L-COSY" (52). In this scheme, a preparation period initiates a single slice-selective 90° RF pulse or a sandwich of slice-selective RF pulses in two orthogonal planes (90°–Δ–180°–Δ) during which the (longitudinal) equilibrium magnetization of nuclear spins is transferred to transverse magnetization or Hahn spin-echo. This is followed by encoding the second spectral dimension with a *variable* time period, t_1, meaning that, during a series of repeat experiments, t_1 takes on a different set of values. This is usually termed the evolution period, which is then followed by a mixing period containing a slice-selective 90° RF pulse in the third orthogonal plane in 2D L-COSY. During this period, there is a coherence transfer between J-coupled spins. In the localized 2D J-resolved spectroscopy (JPRESS), a slice-refocusing 180° RF pulse replaces the slice-selective 90° RF pulse in the L-COSY sequence (49,50). After this, the data acquisition or detection period, t_2, begins in both L-COSY and JPRESS, during which the digitized signal is recorded as a function of t_2, similarly to 1D MRS. This is repeated several times, creating a 2D data matrix, with each row representing a different t_1. This arrayed signal acquisition, $s(t_2, t_1)$, is the basis of 2D spectroscopy and can be extended to further dimensions by combining with two or three spatially encoding gradients, thereby enabling recording of multivoxel 2D spectra in a single slice or a 3D volume. More spectroscopic dimensions will come into play when considering multinuclear MRS. To understand the nature of the interactions between spins during evolution, mixing, and detection periods, and how these events modulate the amplitude, frequency, phase, and full-width at half maximum (FWHM) of the signal, we need to take a closer look at the J-coupled spin-pair system.

A weakly (or strongly) J-coupled spin pair system is defined as one in which the chemical shift differences between magnetically non-equivalent protons ($\delta_I - \delta_S$) within the molecule are larger than (or equal to/less than) the J-coupling between the spins separated by covalent bonds. It can be shown that a general Hamiltonian for J-coupled spins is given by (58)

$$\hat{H} = \Sigma_j \omega_j I_{jz} + \Sigma_{j<k} 2\pi J_{jk} I_j I_k \qquad [1]$$

where a set of spins (I) with different chemical shifts experiences mutual interactions, and ω and J are expressed in rad/s. For a weakly coupled two-spin system (*IS*, two spin-½ particles) with four Zeeman product states in superposition, there are four stationary states or energy levels that represent the fractional population of coupled spins at equilibrium. The allowed transitions in a J-coupled spin pair system are similar to that in an isolated spin system. However, the total magnetic quantum number, m, of only one spin can change by ±1. Hence, there will be four resonances containing two doublets for the *IS* protons with one for the I and the other for the S spin.

2D L-COSY

The 2D signal from spin I acquired along the detection dimension (t_2) is given by (52)

$$s(t_1, t_2) = \mathrm{Tr}[(I_x)\sigma]\exp\left(-i\omega_2{}^{(I)} t_2\right)\exp(-t_1/T_2)\exp(-t_2/T_2)[1 - \exp(-T_R/T_1)] \qquad [2]$$

where

$$\begin{aligned}\sigma \propto & -0.5\cos(2\pi J\Delta)[I_y\cos\left(\omega_1{}^{(I)} t_1\right)\cos(\pi J t_1) + I_x\sin\left(\omega_1{}^{(I)} t_1\right)\cos(\pi J t_1) \\ & +2I_zS_x\cos\left(\omega_1{}^{(I)} t_1\right)\sin(\pi J t_1) - 2I_zS_y\sin\left(\omega_1{}^{(I)} t_1\right)\sin(\pi J t_1)] \\ & +0.5\sin(2\pi J\Delta)[I_y\cos\left(\omega_1{}^{(I)} t_1\right)\sin(\pi J t_1) + I_x\sin\left(\omega_1{}^{(I)} t_1\right)\sin(\pi J t_1) \\ & -2I_zS_x\cos\left(\omega_1{}^{(I)} t_1\right)\cos(\pi J t_1) + 2I_zS_y\sin\left(\omega_1{}^{(I)} t_1\right)\cos(\pi J t_1)]\end{aligned} \qquad [3]$$

T_R, T_1, and T_2 represent repetition time and longitudinal and transverse relaxation times, respectively. It is also evident from Equation [3] that the coherence transfer (CT) from spin I to S is characterized by two-spin operators, $2I_zS_x$ and $2I_zS_y$. A similar equation can be derived for S spin resulting in a coherence transfer to I spin.

Apodization filters for 2D L-COSY

As shown in Equation [3], the first maximum of the CT echo will occur at $t_1 = 1/2J$ for the two-spin system (*IS*) and the position of the maximum for lactate (I_3S, three methyl and one methine protons) will be at $t_1 = \pi/4J$ as described previously by Ziegler *et al.* (60). In a strongly coupled AB spin system such as citrate in the prostate, the coherence transfer function becomes more complicated, since the chemical shift difference is equal to or less than J (50,54,61). It is also evident in Equations [2] and [3] that the 2D diagonal peak intensities follow a cosine dependence and time domain cross-peak amplitudes increase from zero at the beginning to a maximum at $1/2J$ with the signal decay according to T_2*. As discussed by Ernst *et al.*, for small t_1 and t_2 values, the contribution to the 2D cross peak volume is insignificant (57). Hence, it is advisable to weight the time-domain signal, as shown in Equation [2], by a weighting function that will deemphasize the signal for small t_2 and t_1 values (57). While post-processing a 2D L-COSY spectrum, optimal matching filters such as a sine-bell or skewed squared sine-bell can be used along both dimensions for better sensitivity of 2D cross peaks. A sine-bell (SB) filter can be defined as

$$\mathrm{SB}_n = \sin\left\{(\pi/n)\left[1 + (n-1)t_w/\left(t_i{}^{\max} - t_i{}^{\min}\right)\right]\right\} \qquad [4]$$

where n being the shift parameter is a positive integer and i runs over the two dimensions, 1 and 2. For large n, Equation [4] reduces to

$$\mathrm{SB} = \sin\left\{\pi t_w/\left(t_i{}^{\max} - t_i{}^{\min}\right)\right\} \qquad [5]$$

As shown in Equation [5], the symmetric unshifted SB function has a maximum value of 1 at $t_w = (t_i{}^{\max} - t_i{}^{\min})/2$.

As the maximum value can be reached at an earlier time, the shifted SB or its square (SB_n^2) may offer more flexibility than the unshifted ones.

As described by Delikatny *et al*. (62), there are three major advantages with using the SB filter. (1) As it begins with zero value, unlike an exponential filter, it can emphasize cross peaks relative to 2D diagonal peaks that are cosine dependent. (2) It removes the broad wings (dispersive components) from 2D magnitude lineshapes. (3) At the end of the time domain, the trailing edge of the SB function the window function goes smoothly to zero and truncation errors due to apodization are minimized.

Shown in Figure 1(A) is a 2D L-COSY spectrum recorded in the peripheral zone of a 28 y.o. healthy prostate using a 1.5 T whole body MRI/MRS scanner (GE Medical Systems, Waukesha, WI) with an endorectal coil (MEDRAD, Pittsburgh, PA) combined with a pelvic phased-array coil for signal reception. A body RF coil was used for transmitting the RF pulses. A $2\times2\times1\,cm^3$ voxel was placed on the lower left peripheral zone using an axial fast spin-echo MRI. The 2D L-COSY spectrum was recorded using the following parameters: $T_R = 2$ s, minimal $T_E = 30$ ms, 45 t_1 increments and 16 averages. The total acquisition time was 24 min. The raw data was acquired using 1024 complex points and a spectral window of 2500 Hz along the detected direct (t_2) dimension. The incremental period (Δt_1) was 1.6 ms to yield a spectral window of 625 Hz along the second indirect dimension (t_1). The spectral 2D raw files were processed using the FELIX software package (Felix NMR Inc., San Diego, CA). The 2D MRS array was apodized using the skewed squared sine-bell filters (62) along the two axes and before zero-filling to 2048×256. After double Fourier transformation, the 2D L-COSY spectra were reconstructed in the magnitude mode and displayed as contour plots. For comparison, shown in Figure 1B is the same 2D L-COSY data processed using the conventional exponential filter functions (3 Hz), where the emphasis of discriminating 2D cross peaks from the diagonal peaks is completely sacrificed compared with the skewed squared sine-bell filters.

2D JPRESS

In the half-echo sampled 2D JPRESS, two increments ($t_1/2$) are used before and after the last 180° RF pulse (49,50). The 2D signal for spin *I* acquired along the detected dimension (t_2) is the same as shown in Equation [2] with a redefined σ and ω_1. As there is no mixing period here, the 2D JPRESS spectrum contains the same number of peaks as the conventional 1D MRS using the PRESS sequence. The second spin-echo during which the second spectral dimension is encoded will refocus the chemical shift but not in bilinear interaction, *J*, similar to the first Hahn echo. The frequency of each peak along the t_1 dimension will be dependent on *J* only, where the frequency along the t_2 dimension will be (chemical shift $\pm$ 1/2 *J*). A more detailed theoretical explanation is discussed by Thrippleton *et al*. (63).

2D JPRESS of a healthy human prostate

Figure 2(B) shows a 2 ml voxel 2D JPRESS spectrum of the same 28 y.o. healthy prostate as shown in Figure 1. The voxel location of the 2D JPRESS spectrum is shown in Figure 2(A). The 2D peaks due to Cit were located along $F_1 = \pm1.6$ Hz, ±7.9 Hz, and ±17.5 Hz. In addition, the triplet nicely resolved about $F_2 = 3.1$ ppm along $F_1 = 0$ Hz and ±7.8 Hz was identified as Spm. The presence of strong Cit peaks was consistent with the well-known fact of its high abundance in healthy prostate (39,40). Moreover, there were 2D peaks along $F_1 = 0$ Hz due to Cr and Ch at $F_2 = 3.0$ ppm and 3.2 ppm, respectively. The J-resolved peaks due to Ch methylene protons were not observable due to the smaller voxel size and reduced number of averages.

Apodization filters for 2D JPRESS

The J-coupled multiplets are better resolved along the t_1 dimension than the detected t_2 dimension as well the 1D MRS counterpart, since any defocusing linear B_0 interactions including the static field inhomogeneities during the first half of t_1 are

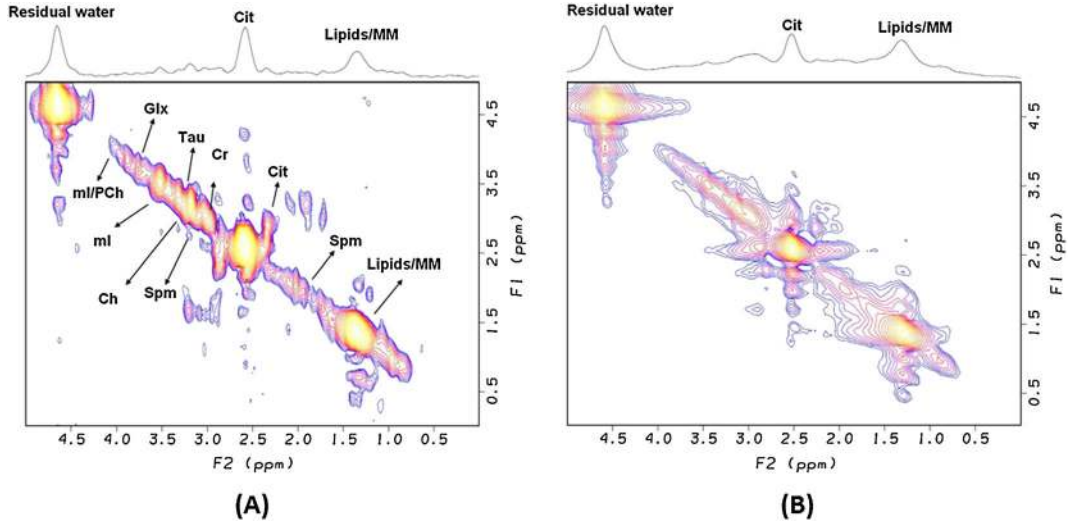

Figure 1. A 1.5 T 2D L-COSY spectrum recorded from a healthy prostate of a 28 y.o. male using two different apodization filters: (A) a skewed squared sine-bell and (B) an exponential filter using a 3 Hz line broadening. The 2D L-COSY spectrum was recorded using the following parameters. A $2\times2\times1\,cm^3$ voxel was placed on the lower left peripheral zone, $T_R = 2$ s, minimal $T_E = 30$ ms, 45 t_1 increments, incremental period (Δt_1) of 1.6 ms to yield a spectral window of 625 Hz along the F_1 dimension, 16 averages per Δt_1, 1024 complex points and a spectral window of 2500 Hz for the F_2 dimension. The total acquisition time was 24 min. An endorectal coil combined with a pelvic phased-array coil for signal "receive" and a body rf coil for "transmit" were used. The raw spectral files were processed using the FELIX software package (Felix NMR Inc., San Diego, CA). After zero-filling to 2048×256, double Fourier transformation was performed and the 2D L-COSY spectra were reconstructed in the magnitude mode and displayed as contour plots.

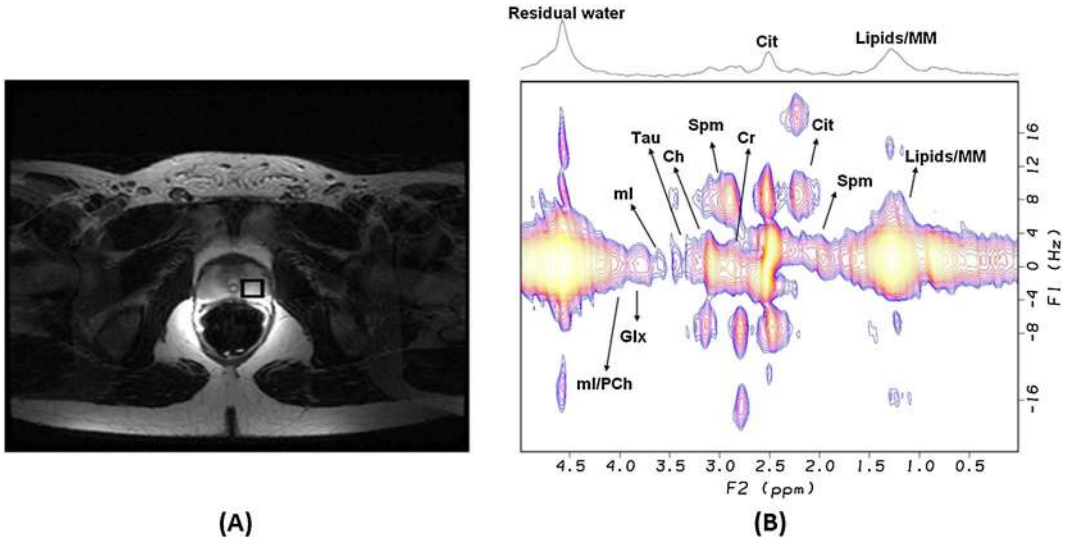

Figure 2. (A) An axial fast spin-echo MRI slice showing the 2D MRS voxel; the MRI acquisition parameters were as follows: 4 mm slice, $T_R = 2.5$ s, $T_E = 84$ ms, FOV = 14–24 cm, acquisition matrix 256 × 192, and 4 number of excitations (NEX), resulting in an acquisition time of 4 min. (B) A half-echo sampled 1.5 T 2D JPRESS spectrum recorded in the peripheral zone of the same 28 y.o. healthy prostate as used for Figure 1 using the following parameters: $2 \times 2 \times 1$ cm^3 voxel, $T_R = 2$ s, minimal $T_E = 30$ ms, 45 t_1 increments, incremental period (Δt_1) of 10 ms (5 ms before and 5 ms after the last 180° RF pulse) to yield a spectral window of ±50 Hz along the F_1 dimension, 16 averages per Δt_1, 1024 complex points and a spectral window of 2500 Hz for the F_2 dimension. The total acquisition time was 24 min.

refocused during the second half, resulting in a net zero dependence on the B_0 static field inhomogeneities and other linear interactions. Even though this is a major advantage, the phase-modulated time domain datasets are transformed into phase-twisted 2D peaks after the double fast Fourier transformation (FFT) of the 2D JPRESS raw data. Hence, the above mentioned squared or simple sine-bell filter functions can be used prior to the double FFT.

Strong coupling effects in 2D JPRESS

It was demonstrated earlier that 2D JPRESS spectra of brain and prostate metabolites show more cross peaks than those of weakly coupled ones (50,54). Shown in Figure 3 is a simulated hard pulse version of the 2D JPRESS (90°–180°–180°) spectrum of Cit using the GAMMA simulation library (64). Cit has two equivalent methylene groups. Each proton pair forms a strongly J-coupled AB spin system (50,54), resulting in eight J-resolved 2D peaks anti-symmetric about $F_2 = 2.65$ ppm, as evident in the experimental and simulated 2D spectra. The 2D peaks located along $F_1 = \pm 1.6$ Hz, ±7.8 Hz, and ±16.4 Hz were in agreement with a previous report (54). Besides, the projected 1D spectra onto F_1 and F_2 axes are also shown.

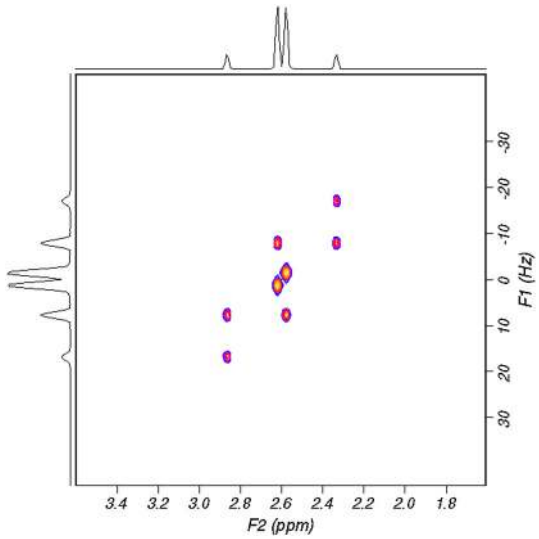

Figure 3. A simulated 1.5 T 2D JPRESS spectrum of citrate using $J = 15.6$ Hz and $\delta = 9.6$ Hz at 1.5 T ($T_R = 2$ s, $T_E = 30$ ms, 256 F_1 points, and 4096 F_2 points).

2D JPRESS of PCa patients with two different Gleason scores (GS)

Figure 4 shows 2D JPRESS spectra recorded in a 59 y.o. BPH and a 50 y.o. PCa patient using a Siemens 1.5 T Avanto MRI scanner. The metabolites such as Cit, Ch, Cr, and Spm were identified and the 2D multiplet patterns of Cit and Spm in JPRESS spectra were detected with a reasonable resolution. However, the limited spectral resolution along the second axis (F_1) resulted in an overcrowded 2D JPRESS spectrum. This complex spectrum is due to the strong coupling effects of Cit as presented in Figure 3. Nagarajan *et al*. (56) have shown a decrease of Spm in PCa patients of higher GS (4 + 3) compared with lower GS (3 + 4) using 2D J-resolved spectroscopy. High levels of Spm are found in the healthy prostatic ducts (65–67) and the observed variations of Spm in cancer may be due to the loss of ductal morphology or a reduction in the secretion of polyamines (68). The Spm itself, which plays a role in cell proliferation and differentiation, may provide additional information for early diagnosis and prognosis predicting tumor progression. However, the separation of Ch from Spm is inherently difficult because of the proximity of the peaks and the limited spectral resolution available within a reasonable imaging time. A distinct integration region cannot be assigned for Spm. Thus, polyamine level could not be integrated and quantified unambiguously using operator

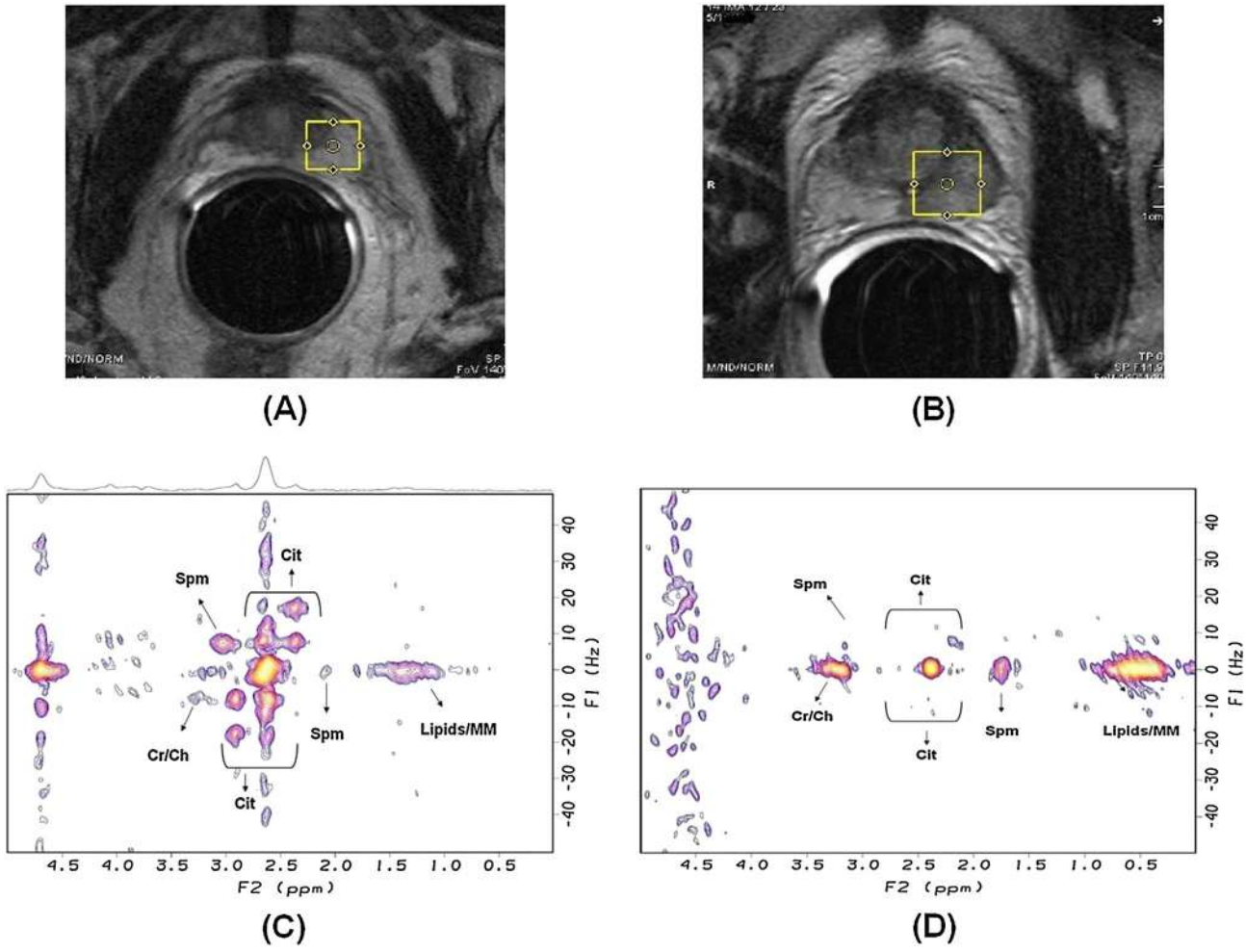

Figure 4. T_2-weighted axial MRI slice images showing locations of 2D JPRESS spectra recorded in the peripheral zones of (A, C) a 59 y.o. BPH patient and (B, D) a 50 y.o. prostate cancer patient. The half-echo sampled 2D JPRESS spectra were recorded using the following parameters: a 1.5 T MRI scanner, $T_R = 2$ s, minimal $T_E = 30$ ms, 64 t_1 increments, incremental period (Δt_1) of 10 ms (5 ms before and 5 ms after the last 180° RF pulse) to yield a spectral window of ±50 Hz along the F_1 dimension, eight averages per Δt_1, 2048 complex points and a spectral window of 2000 Hz for the F_2 dimension. The total acquisition time was 16 min. The raw spectral files were processed using the FELIX software package (Felix NMR Inc., San Diego, CA). After zero-filling to 2048 × 256, double Fourier transformation was performed and the 2D JPRESS spectra were reconstructed in the magnitude mode and displayed as contour plots.

defined peak volumes in the frequency domain. It can be only assessed qualitatively and reported relative to the choline peak. In the prostate, Spm has three multiplets at 1.8 ppm, 2.1 ppm, and 3.05–3.15 ppm. The 3.05–3.15 ppm multiplet occurs between the Cr and Ch singlets and cannot be entirely resolved from them. Although this ratio has been traditionally called the (Ch+Cr)/Cit ratio, it actually includes Spm also. This presents a problem when Ch is elevated in cancer and Spm is diminished. This hinders accurate quantification of both metabolites. Application of localized 2D JPRESS was also reported in prostate *in vivo* studies by another group (69).

Maximum-echo sampled 2D JPRESS

In the half-echo sampled 2D JPRESS, if the incremental period (Δt_1) typically used is 10 ms, the resulting total echo time duration will be 630 ms to achieve a spectral window of 100 Hz along F_1. This would lead to severe T_2 attenuation of 2D peaks, resulting in a significant signal loss. It is known that T_2 value of several metabolites are shorter at 3 T than 1.5 T (70,71), which would lead to further attenuation of J-resolved 2D peaks at higher field strength. As reported by Schulte *et al*. recently, a maximum-echo based JPRESS can sample the echo signals starting immediately after the final crusher gradient of the last 180° pulse (72). This acquisition scheme has several advantages over the half-echo sampling data presented in the previous section, where the acquisition starts at the echo top.

A common definition of the sensitivity is the signal-to-noise (SNR) ratio per unit time for identical experimental durations and a constant acquisition time window; the noise will remain the same and it is sufficient to compare the signal. The signal is commonly defined as the peak height in the frequency domain, which is equivalent to the integral of the time domain signal. For single resonances, it suffices to integrate over the exponential damping curve of the echo along the times t_1 and t_2.

As described by Schulte *et al*., the efficiency of 2D experiments can be compared with 1D PRESS by integrating over the indirect dimension (t_1). The maximum-echo sampled JPRESS signal can be divided into two halves (72). The damping curve in the traditional half-echo sampling JPRESS is equivalent to the right

half as shown in the following equation:

$$\int^{T_{s1}}\int^{\infty}\exp(-t_2/T_2^*)\exp(-t_1/T_2)\,dt_2dt_1 = T_2^*T[1-\exp(-T_{s1}/T_2)] \quad [6]$$

where T_{sI} represents the total sampling time along t_1.

Adding both halves together, the total signal of the maximum-echo sampled JPRESS can be written as

$$2T_2^*T_2[1-\exp(-T_{s1}/T_2)] - T_2^*t_x[1-\exp(-T_{s1}/t_x)] \quad [7]$$

where

$$t_x = 2T_2T_2^*/(T_2+2T_2^*) \quad [8]$$

In contrast, the equation for the 1D PRESS sequence with the shortest TE equivalent to the 2D JPRESS at $t_1 = 0$ can be written as the following:

$$\int^{T_s}\int^{\infty}\exp(-t_2/T_2^*)\,dt_2dt_1 = T_2^*T_{sI} \quad [9]$$

The ratio of maximum-echo sampled JPRESS to PRESS is given by

$$2T_2/T_{s1}[1-\exp(-T_{s1}/T_2)] - t_x/T_{s1}[1-\exp(-T_{s1}/t_x)] \quad [10]$$

and half-echo JPRESS to PRESS (Equation [9]) by

$$T_2/T_s[1-\exp(-T_{sI}/T_2)] \quad [11]$$

As presented by Schulte *et al.*, the maximum-echo sampled JPRESS scheme has optimal sensitivity in 2D experiments and it has the same sensitivity as the 1D PRESS at long $T_2 > 200$ ms, which is the case for singlets from Cr and trimethyl protons of Ch (72).

Shown in Figure 5 is maximum-echo sampled 2D JPRESS data acquired in a 27 y.o. healthy male before (A) and after (B) a phase rotation using the following parameters: a voxel of $2\times2\times2$ cm^3, $T_R/T_{Emin} = 2$ s/30 ms, 2048 complex points for the detected t_2 dimension sampling a spectral width of 2000 Hz, 100 Δt_1 increments before the last 180° slice-selective RF pulse with each $\Delta t_1 = 1$ ms, eight averages per Δt_1, a 3 T MRI scanner, 16 channel body matrix coil for "receive" and a quadrature body "transmit" coil. This is in agreement with what was shown by Lange *et al.* (69).

ECHO-PLANAR CORRELATED AND J-RESOLVED SPECTROSCOPIC IMAGING

The single-voxel (SV)- based 1D and 2D MRS studies suffer from limited spatial coverage due to recording of one voxel per measurement. In contrast, the 2D or 3D MRSI technique would facilitate adequate spatial coverage in a single recording. However, a major limitation of the conventional 2D/3D MRSI technique stems from using incremented phase encoding for two or three directions to traverse the *k*-space and the total scan time required for the acquisition of a high-resolution 3D MRSI data may be prohibitively long for clinical exams. Another drawback is that only four major metabolites (Cit, Cr, Spm, and Ch) have been detected by the 3D MRSI sequence due to long T_E for optimal suppression of water and lipids. The acquisition of fully phase-encoded MRSI can be greatly shortened by using echo-planar spectroscopic imaging (EPSI), a method originally proposed by Mansfield (73), in which a time varying readout gradient encodes spatial and spectral dimensions during a single readout. Much effort has been devoted to implementing EPSI (74–78), the results of which have shown sufficient SNR. In the last few years, two different fast MRSI sequences have been demonstrated with potential applications in PCa. First, the flyback echo-planar read-out trajectories were incorporated by Chen *et al.* into the PRESS sequence using composite RF pulses with high-quality MRSI data recorded in nine PCa patients (79). Second, high-resolution EPSI was implemented on a 4.7 T MRI scanner with the sequence tested in animal models of PCa (80).

To overcome a major limitation of the SV localized 2D MRS, phase-encoding gradients can be combined with L-COSY and JPRESS to record multivoxel 2D spectra in human tissues. However, the total duration will be impractically long due to four different increments for encoding: one for the second spectral dimension and three for the three spatial dimensions. With the above mentioned progress in accelerating one spatial and

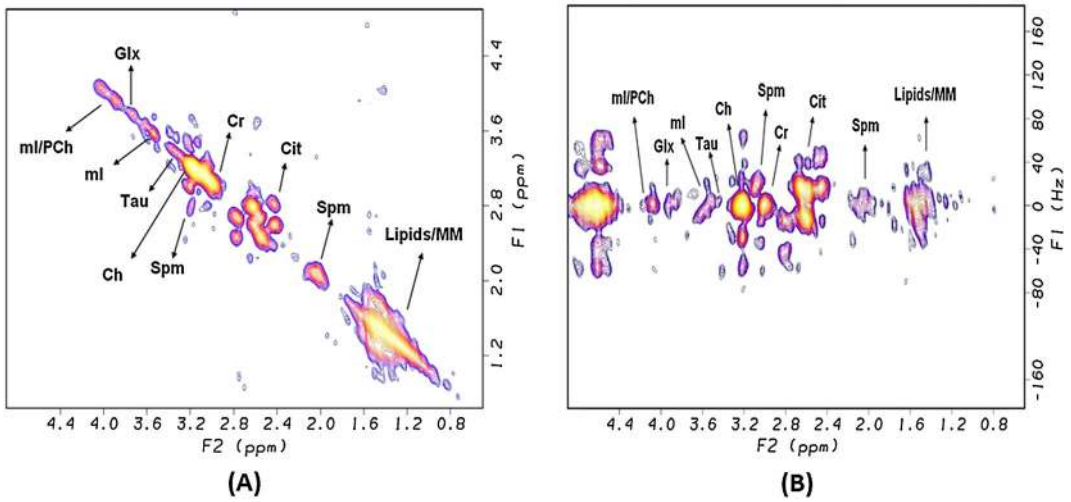

Figure 5. A maximum-echo sampled 2D JPRESS spectrum recorded in the peripheral zone of A 27 y.o. healthy prostate using a 3 T MRI scanner after (A) a double FFT of the 2D raw matrix and (B) a double FFT after incorporating the phase rotation of the raw matrix to impose the evolution after the last 180° slice-selective RF pulse.

spectral coverage using the 3D EPSI, the 2D L-COSY and JPRESS sequences were recently modified with an EPSI type of readout to yield 2D spectra from multiple voxels in a single experiment, called echo-planar correlated spectroscopic imaging (EP-COSI) (81) and echo-planar J-resolved spectroscopic imaging (EP-JRESI) (82), respectively. The EP-COSI and EP-JRESI sequences use a bipolar spatial read-out train facilitating simultaneous spatial and spectral encoding, and the conventional phase and spectral encodings for the remaining spatial and indirect spectral dimensions. Multiple 2D COSY and 2D J-resolved spectra were recorded over the spatially resolved volume of interest (VOI) localized by a train of three slice-selective RF pulses (90°–180°–90°) and (90°–180°–180°). These two techniques can be used to detect and quantify metabolites with less T_2 weighting than the earlier 3D MRSI sequences using conventional phase encoding because of the shorter echo time. Figure 6 shows the four-dimensional (2D spectral + 2D spatial) EP-COSI data recorded in a 27 y.o. healthy volunteer. The voxel placement is shown in Figure 6(A) and the multivoxel display of Cr, Ch, and Spm over the localized VOI in Figure 6(B). An extracted 3 ml 2D COSY spectrum is displayed in Figure 6(C).

A 500 ml prostate phantom was prepared containing the following metabolites at physiological concentrations as reported in healthy human prostate (69): Cit (50 mM), Cr (5 mM), Ch (1 mM), Spm (6 mM), mI (10 mM), PCh (2 mM), taurine (Tau, 3 mM), Glu (4 mM), Gln (2.5 mM) and scyllo-inositol (Scy, 0.8 mM). Here, we show that all of the above mentioned metabolites can be detected using fully encoded EP-JRESI data. Shown in Figure 7(A) is an axial MRI slice image showing the multivoxel grids of MRSI with the yellow boundary of the field of view (FOV), and the white box representing the volume of interest (VOI) localized by the PRESS sequence which is an integral part of the EP-JRESI sequence (82). The following parameters were used for acquiring the 4D EP-JRESI data: T_R/T_E = 1500 ms/30 ms, 16 phase encodes (k_y), 32 read-out points (k_x) with oversampling, 512 ± read-out trains resulting in 512 pairs of complex spectral points in the second spectral dimension (t_2), 100 t_1 increments for the indirect spectral dimension and one average per encoding. A total duration of 40 min was necessary to acquire this water-suppressed 4D EP-JRESI data. A non-water-suppressed EP-JRESI data using four averages with only one t_1 increment was used for eddy current and phase correction of the suppressed data (81). After apodization and Fourier transformation of this 4D data, the reconstructed 2D J-resolved spectra were overlaid on top of the 16 × 16 spatial grids. An extracted 2D J-resolved spectrum (3 ml) around the center of the VOI is shown in Figure 7(B). The diagonal peaks cutting through $F_1 = 0$ show all singlets contained in a 1D PRESS spectrum and the 2D cross (off-diagonal) peaks of J-coupled metabolites such as Cit, Spm, Glu, Gln, and mI were also clearly visible.

MULTI ECHO (ME) BASED ECHO-PLANAR J-RESOLVED SPECTROSCOPIC IMAGING (MEEP-JRESI)

Multi-echo (ME) encoding schemes, namely turbo spin echo (TSE) and fast spin echo (FSE), have been shown to decrease the overall scan time in MRI (83–85). Similar approaches have demonstrated the applicability of ME techniques to MRSI (86,87). One limiting factor for ME-based MRSI is the T_2 decay as the signal is greatly diminished with each echo, especially in living tissues, where T_2 relaxation times are shorter (70,71,88). Recently, a 4D EP-JRESI sequence was implemented combining two spectral dimensions with two spatial dimensions and incorporating multi-echo (ME) for encoding one of the spatial dimensions to reduce scan times to suit clinical requirements. Nagarajan *et al*. (89) employed the MEEP-JRESI sequence on a 3 T MRI/MRS scanner and evaluated it in three healthy prostate volunteers using the external body matrix "receive' coil. The MEEP-JRESI technique facilitates recording multivoxel 2D J-resolved spectra in a single recording using a total acquisition time of approximately 13 min. Figure 8(A) shows the T_2-weighted axial MRI displaying the VOI location for the MEEP-JRESI recorded in a 28 y.o. healthy volunteer. A multivoxel display of Cr/Ch/Spm inside the VOI is shown in Figure 8(B) with each voxel resolution of 2 ml.

4D EP-JRESI AND EP-COSI: ACCELERATED ACQUISITION AND COMPRESSED SENSING RECONSTRUCTION

Image acquisition approaches have conventionally followed the Nyquist–Shannon sampling theorem, where the sampling rate

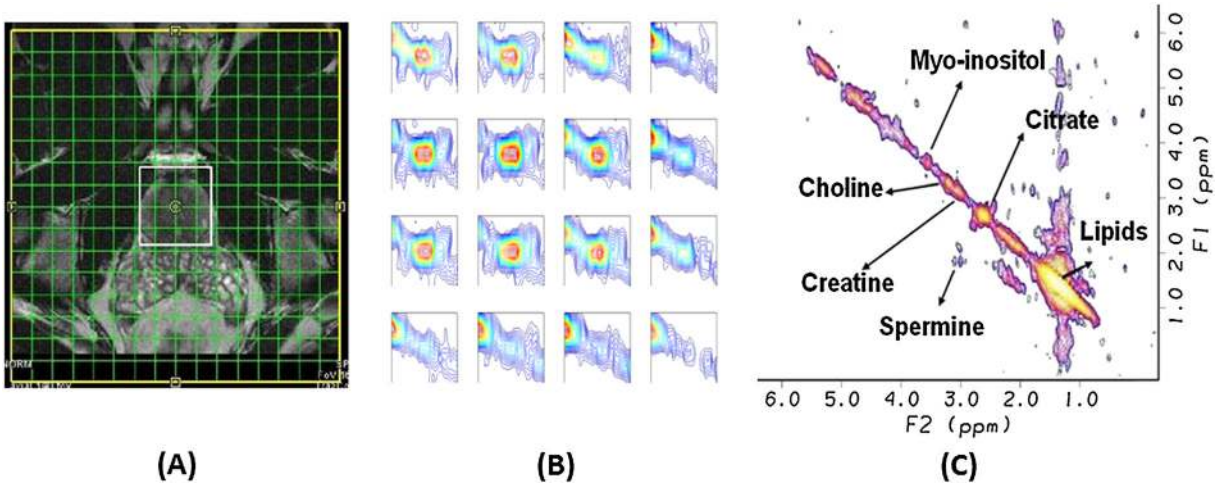

Figure 6. (A) T_2-weighted axial MRI of 27 y.o. healthy volunteer with MRSI voxel location using a 3 T MRI scanner and (B) multivoxel distribution of Cr, Ch, and Spm peaks extracted from the EP-COSI data. (C) 2D L-COSY spectrum extracted from the EP-COSI data of a 27 y.o. healthy male.

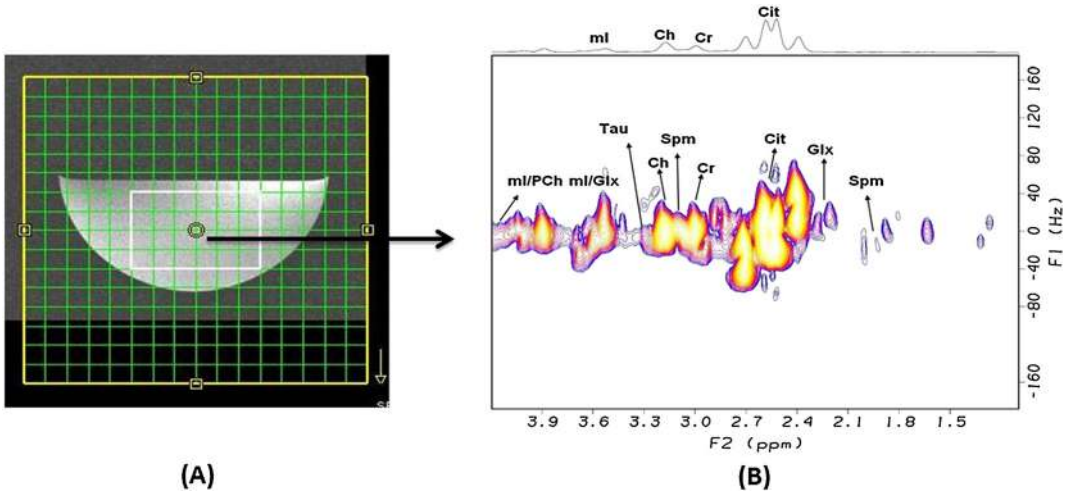

Figure 7. (A) An axial slice MRI of a prostate phantom containing 10 metabolites; (B) an extracted 2D J-resolved spectrum (voxel size of 3 ml). A 3 T MRI scanner was used.

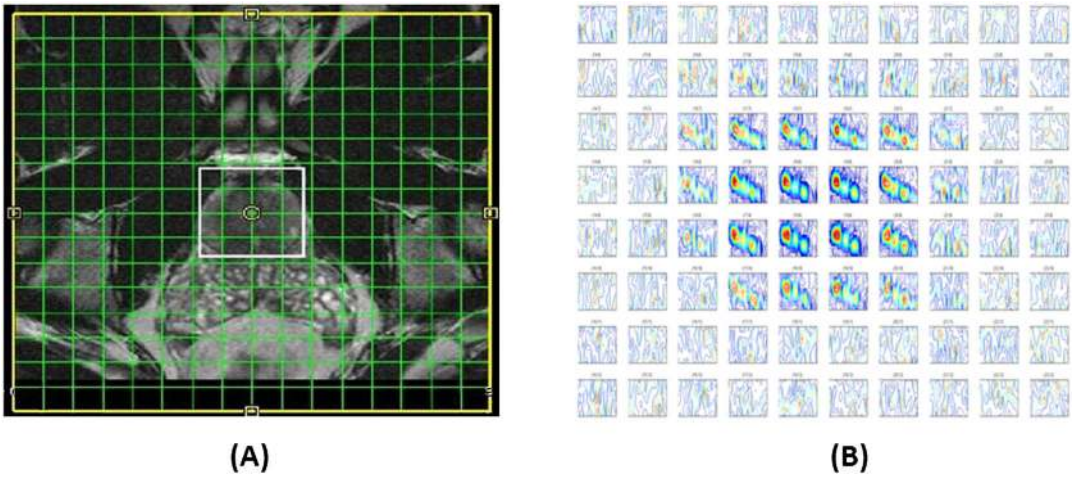

Figure 8. (A) The T_2-weighted axial MRI and (B) multivoxel distribution of Cr, Ch, and Spm from a 28 y.o. healthy prostate from MEEP-JRESI. A 3 T MRI scanner was used.

should be at least twice the maximum frequency present in the signal of interest. However, the theory of compressive sensing (CS) describes a combined sampling and reconstruction paradigm which states that certain images and signals can be recovered from an acquisition that uses fewer samples than required by Nyquist–Shannon (90,91). Since the annual meeting of the International Society for Magnetic Resonance in Medicine in May 2007, CS has met with significant enthusiasm among MR researchers (92–96). Three criteria are critical for the successful application of CS (92): (1) the data should have a sparse representation in a particular transform domain, (2) the aliasing from undersampling should be incoherent in that transform domain and (3) a nonlinear reconstruction should be used to enforce both the sparsity of the reconstruction and consistency with the measurements. MRI is well suited for CS, and there are significant benefits in imaging speed and reduced costs, thereby improving patient care. A major challenge in designing CS data acquisition methods for MRI is in implementing NUS densities that result in incoherent aliasing while providing data sparsity in a transform domain, such as wavelets, curvelets, etc (76). Incoherent aliasing combined with sparsity in the transform domain allows L1-norm-based reconstructions from NUS data to be exact under ideal conditions and "approximately" exact under normal conditions (90,91). Application of CS sampling and reconstruction has been accomplished in parallel imaging to exploit both image sparsity and coil sensitivity encoding (97). As described earlier, there are three spatial encodings and one spectral encoding in a 3D MRSI sequence, and recently Vigneron and co-workers developed an undersampling scheme along both spatial encoded dimensions to achieve suitable incoherent aliasing. They have demonstrated a factor of two enhancement in the spatial resolution without increasing acquisition time or decreasing coverage (94). A further modified scheme was shown to provide up to a acceleration factor of 7.5 for hyperpolarized MRSI (98).

The total duration of a fully encoded 3D MRSI can be approximately 2 hours if the following parameters are used: $T_R = 1$ s, $12 \times 12 \times 12$ for phase-encoding along three spatial dimensions and four averages. Therefore, average weighted and other schemes have been used to minimize the total time (99). During the last five years, two different fast MRSI sequences have been demonstrated for PCa as mentioned earlier (79,80). There has

been one report of combining two spectral dimensions with 2D spatial encoding applicable to PCa (100). As discussed earlier, a second spectral dimension was added to the EPSI technique in the recently published 4D EP-COSI sequence (81). A total scan time of 40 min was required for 512×100 complex points along the two spectral dimensions with a 16×16 spatial resolution along the two spatial dimensions.

We demonstrate here that by imposing a NUS scheme on the above presented fully sampled data shown in Figure 7(B) and after the CS reconstruction, the quality of the extracted 2D MRS spectra from the undersampled data is comparable to that of the fully sampled data. Therefore, NUS was imposed on one spectral and one spatial dimension and the remaining spectral and spatial dimensions were fully sampled by the EPI readout. Compared with the fully encoded data, the 25% NUS densities demonstrate 4× undersampling, which reduced total scan duration to 10 min. Figure 9 shows the multivoxel EP-JRESI data (A) and extracted 2D J-resolved spectrum (B) after the CS reconstruction, demonstrating the fidelity of the CS reconstruction.

The feasibility of recording a 25% sparsely sampled *in vivo* EP-JRESI data and successful CS reconstruction of the 2D J-resolved spectrum is demonstrated here. A 32 y.o. healthy human subject was investigated on the 3 T MRI scanner using the quadrature body coil "transmit" and external body matrix "receive" coil assembly. The following parameters were used to acquire the NUS sampled EP-JRESI data: $T_R/T_E = 1.5\,\text{s}/30\,\text{ms}$, 2 averages, $512\,t_2$, oversampled 32 k_x, 25% NUS along the indirect spectral (t_1) and spatial k_y dimensions. In Figure 10(A), an axial MRI of the abdomen is shown displaying the VOI covering the prostate localized by the PRESS sequence and the EP-JRESI grids. The split-Bregman iterative algorithm (101) was used to reconstruct the missing t_1 and k_y data points from the prospectively undersampled data matrix. The CS-reconstructed multivoxel display confirmed the feasibility of detecting prostate metabolites over many voxels. The CS-reconstructed 2D J-resolved spectrum extracted from the central location is shown in Figure 10(B). The 2D diagonal and cross peaks of Cit and other metabolites are visible as reported in a recent publication (102). The endorectal "receive" coil is expected to facilitate at least one order of magnitude higher sensitivity than that of the body matrix assembly used here. Hence, significantly improved sensitivity can be achieved using the endorectal coil. Our recent findings on the endorectal coil-based NUS EP-JRESI acquisition and CS reconstruction confirming the improved detectability of prostate metabolites will be published elsewhere.

PRIOR-KNOWLEDGE FITTING FOR QUANTITATION OF PROSTATE METABOLITES

As discussed earlier, previous attempts by other researchers using the single- and multivoxel-based 1D MRS approaches have reported four prostate metabolites only, such as Cit, Ch, Spm, and Cr (10,11). This was due to the long echo time ($T_E > 100$ ms) and limited 1D spectral quantitation approaches used. Recent investigations of HR-MAS of *ex vivo* prostate cancer specimens on ultra-high field NMR spectrometers have demonstrated quantitation of many more metabolites such as Tau, mI, scyllo-inositol (sI), Glx, etc. than what has previously been shown using the 1D MRS *in vivo* approaches so far (103–105). A recent report has used prior-knowledge-based LC-model processed HR-MAS *ex vivo* data to quantify additional metabolites such as Glx and glucose (106). A few years ago, Schulte *et al.* developed a prior-knowledge fitting (ProFit) algorithm and demonstrated the feasibility of quantitation of brain and prostate metabolites (69,72,107). After the fitting process, the quality of the fit can individually be evaluated for each metabolite using Cramér–Rao lower bounds (CRLB) (108). A statistical lower bound for the achievable standard deviation of the estimated parameters is provided by CRLB which are not dependent on the individual concentrations but only on the noise and the orthogonality of the basis function. The architecture of the fitting process allows for another useful measure of the quality of the fitting of the spectrum by comparing creatine 3.9 (Cr3.9) to creatine 3.0 (Cr3.0) ratios, which ideally should be 1 since the number of protons (2,3) are already taken into account for Cr3.9 and Cr3.0, respectively, in their basis-set creation. Higher Cr3.9/Cr3.0 ratios reflect poor spectra and implying that the results can be excluded. Note that in order to implement this control creatine 3.9 and creatine 3.0 have to be implemented as different elements in the basis sets. Our preliminary

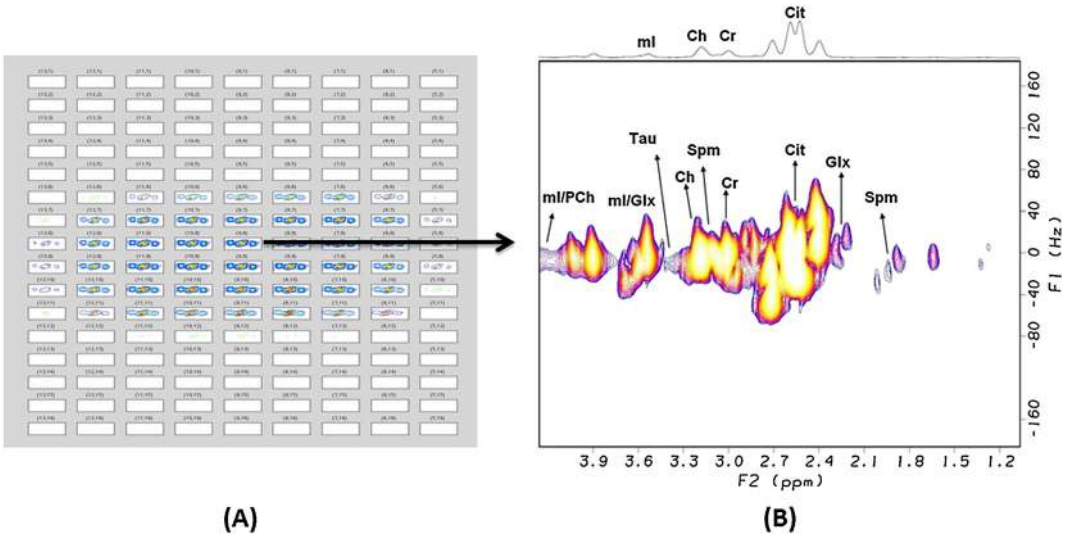

Figure 9. (A) The CS-reconstructed 2D J-resolved multivoxel spectra showing the Cit multiplets processed from the 25% NUS raw data using a 3 T MRI scanner. (B) the corresponding 2D J-resolved spectrum extracted from the center voxel.

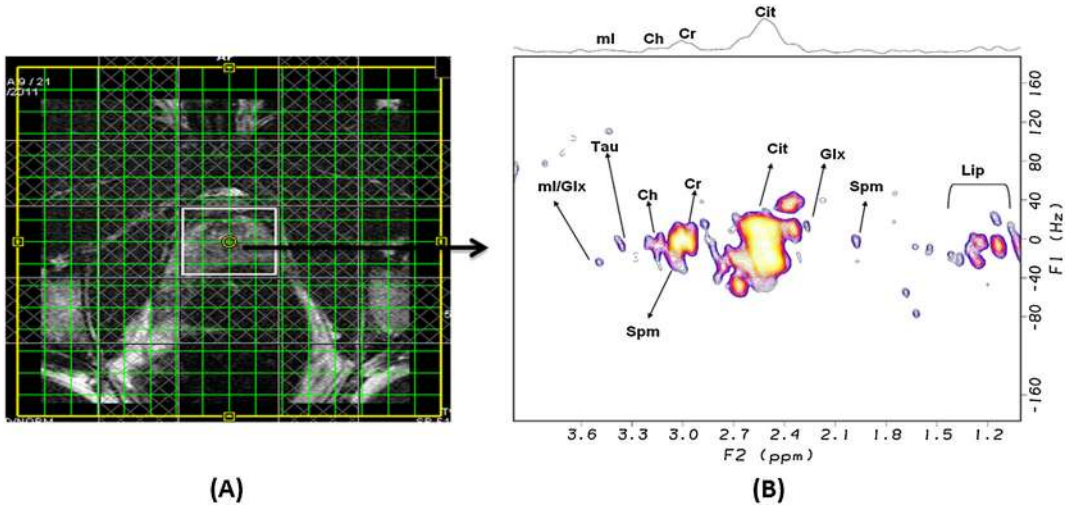

Figure 10. (A) An axial MRI slice of the 32 y.o. healthy male subject showing the VOI and MRSI grids. (B) The 2D J-resolved spectrum extracted from a 2 ml voxel. A 3 T MRI scanner was used.

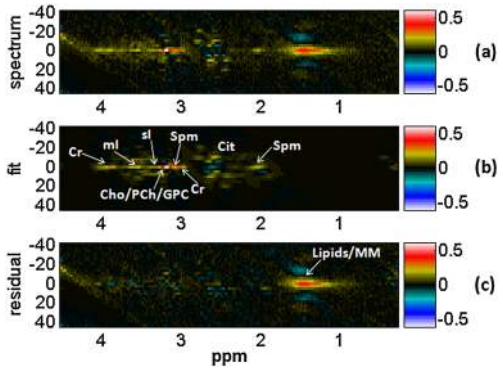

Figure 11. ProFit fitting of 2D JPRESS: (a) a 2D JPRESS spectrum recorded in the peripheral zone of the 27 y.o. healthy prostate using a 3 T MRI scanner, (b) its fit and (c) the fit residue as determined with ProFit.

results using the ProFit-based quantitation of the previously acquired GE 1.5 T and Siemens 3 T and 1.5 T MRS data using 2D localized-correlation spectroscopy (L-COSY) spectral acquisition in selected brain pathologies demonstrate the increased power of estimating more brain metabolites such as glutathione (GSH), PCh, PE, and GPC (109,110). Shown in Figure 11 are plots showing the fitting of a 2D JPRESS prostate spectrum (a) using a Siemens 3 T MRI scanner, the same as shown in Figure 5, its fit (b) and the fit residue (c) as determined with the ProFit algorithm. The estimated metabolite ratios (/Cr) using the ProFit quantitation were as follows: Cit, 7.36; PCh, 0.09; GPC, 0.48; Spm, 8.55; mI, 3.79; sI, 0.12; Glu, 1.52; Gln, 0.03; Tau, 1.47. These values were in agreement with the work published by Lange *et al.* (69). However, the applicability of ProFit in a clinical setting is yet to be demonstrated.

FUTURE DIRECTIONS: CLINICAL APPLICATIONS

As discussed above, localized 2D MRS has left infancy and moving to maturity. Twenty minutes of total duration were required for recording the decade old single-voxel-based 2D L-COSY and 2D JPRESS spectra. Recent fully sampled multivoxel-based 4D EP-JRESI and EP-COSI sequences enable recording 2D COSY and J-resolved spectra in multiple regions. However, the total duration was typically 20–40 min depending on the number of incremented spectral (t_1) and spatial encoding (k_y) steps. Recent developments from our group demonstrate clearly that further acceleration can be accomplished using the NUS schemes and total durations of the 4D EP-JRESI and EP-COSI sequences can be shortened to approximately 10 min or less. The nonlinear CS reconstruction is necessary for processing the NUS 4D data. Further work is necessary to demonstrate the potential of multidimensional MR spectroscopic imaging using the fast imaging methods as reported recently to bring it into the clinic as a robust diagnostic metabolite imaging technique. We hope all these recent developments will lead to clinical realization of these novel MRSI sequences in the near future.

Acknowledgements

This work was partially supported by an IDEA grant from the US Army Department of Defense (DOD) Prostate Cancer Research Program (PCRP), grant number W81XWH-11-1-0248. The authors would like to acknowledge the scientific support of Dr. Jonathan Furuyama, Mr. Neil Wilson and Mr. Brian Burns with the NUS-based acquisition schemes and post-processing using CS algorithms.

REFERENCES

1. Jemal A, Siegel R, Xu J, Ward E. Cancer statistics, 2010. CA Cancer J. Clin. 2010; 60(5): 277–300.
2. Gerber GS, Chodak GW. Routine screening for cancer of the prostate. J. Natl. Cancer Inst. 1991; 83(5): 329–335.
3. Gleason DF, Mellinger GT. Prediction of prognosis for prostatic adenocarcinoma by combined histological grading and clinical staging. J. Urol. 1974; 111(1): 58–64.
4. Amin M, Boccon-Gibod L, Egevad L, Epstein JI, Humphrey PA, Mikuz G, Newling D, Nilsson S, Sakr W, Srigley JR, Wheeler TM, Montironi R. Prognostic and predictive factors and reporting of prostate carcinoma in prostate needle biopsy specimens. Scand. J. Urol. Nephrol. 2005; 216: 20–33.
5. Carvalhal GF, Smith DS, Mager DE, Catalona WJ. Digital rectal examination for detecting prostate cancer at prostate specific antigen levels of 4 ng/mL or less. J. Urol. 1999; 161(3): 835–839.
6. Eastham JA, May R, Robertson JL, Sartor O, Kattan MW. Development of a nomogram that predicts the probability of a positive prostate biopsy in men with an abnormal digital rectal

examination and a prostate-specific antigen between 0 and 4 ng/mL. Urology 1999; 54(4): 708–713.
7. Catalona WJ, Richie JP, Ahmann FR, Hudson MA, Scardino PT, Flanigan RC, deKernion JB, Ratliff TL, Kavoussi LR, Dalkin BL, Waters WB, MacFarlane MT, Southwick PC. Comparison of digital rectal examination and serum prostate specific antigen (PSA) in the early detection of prostate cancer: results of a multicentre clinical trial of 6,630 men. J. Urol. 1994; 151(5): 1283–1290.
8. Schröder FH, van der Maas P, Beemsterboer P, Kruger AB, Hoedemaeker R, Rietbergen J, Kranse R. Evaluation of the digital rectal examination as a screening test for prostate cancer. Rotterdam section of the European Randomized Study of Screening for Prostate Cancer. J. Natl. Cancer Inst. 1998; 90(23): 1817–1823.
9. Schröder FH, Carter HB, Wolters T, van den Bergh RC, Gosselaar C, Bangma CH, Roobol MJ. Early detection of prostate cancer in 2007. Part 1: PSA and PSA kinetics. Eur. Urol. 2008; 53(3): 468–477.
10. Kurhanewicz J, Vigneron D, Carroll P, Coakley F. Multiparametric magnetic resonance imaging in prostate cancer: present and future. Curr. Opin. Urol. 2008; 18(1): 71–77.
11. Kurhanewicz J, Swanson MG, Nelson SJ, Vigneron DB. Combined magnetic resonance imaging and spectroscopic imaging approach to molecular imaging of prostate cancer. J. Magn. Reson. Imaging 2002; 16(4): 451–463.
12. Schiebler ML, Tomaszewski JE, Bezzi M, Pollack HM, Kressel HY, Cohen EK, Altman HG, Gefter WB, Wein AJ, Axel L. Prostatic carcinoma and benign prostatic hyperplasia: correlation of high-resolution MR and histopathologic findings. Radiology 1989; 172: 131–137.
13. Berman CG, Brodsky NJ. Prostate cancer imaging. Cancer Control 1998; 5: 541–554.
14. Beyersdorff D, Taupitz M, Winkelmann B, Fischer T, Lenk S, Loening SA, Hamm B. Patients with a history of elevated prostate-specific antigen levels and negative transrectal US-guided quadrant or sextant biopsy results: value of MR imaging. Radiology 2002; 224: 701–706.
15. Le Bihan D, Breton E, Lallemand D, Aubin ML, Vignaud J, Laval-Jeantet M. Separation of diffusion and perfusion in intravoxel incoherent motion MR imaging. Radiology 1988; 168: 497–505.
16. Miao H, Fukatsu H, Ishigaki T. Prostate cancer detection with 3-T MRI: comparison of diffusion-weighted and T2-weighted imaging. Eur. J. Radiol. 2007; 61: 297–302.
17. Lim HK, Kim JK, Kim KA, Cho KS. Prostate cancer: apparent diffusion coefficient map with T2-weighted images for detection – a multireader study. Radiology 2009; 250: 145–151.
18. Mazaheri Y, Hricak H, Fine SW, Akin O, Shukla-Dave A, Ishill NM, Moskowitz CS, Grater JE, Reuter VE, Zakian KL, Touijer KA, Koutcher JA. Prostate tumor volume measurement with combined T2-weighted imaging and diffusion weighted MR: correlation with pathologic tumor volume. Radiology 2009; 252: 449–457.
19. Carmeliet P, Jain RK. Angiogenesis in cancer and other diseases. Nature 2000; 407: 249–257.
20. Padhani AR, Husband JE. Dynamic contrast-enhanced MRI studies in oncology with an emphasis on quantification, validation and human studies. Clin. Radiol. 2001; 56: 607–620.
21. Bigler SA, Deering RE, Brawer MK. Comparison of microscopic vascularity in benign and malignant prostate tissue. Hum. Pathol. 1993; 24: 220–226.
22. Kiessling F, Lichy M, Grobholz R, Heilmann M, Farhan N, Michel MS, Trojan L, Ederle J, Abel U, Kauczor HU, Semmler W, Delorme S. Simple models improve the discrimination of prostate cancers from the peripheral gland by T1-weighted dynamic MRI. Eur. Radiol. 2004; 14: 1793–1801.
23. Mydlo JH, Kral JG, Volpe M, Axotis C, Macchia RJ, Pertschuk LP. An analysis of microvessel density, androgen receptor, p53 and HER-2/neu expression and Gleason score in prostate cancer: preliminary results and therapeutic implications. Eur. Urol. 1998; 34: 426–432.
24. Schlemmer HP, Merkle J, Grobholz R, Jaeger T, Michel MS, Werner A, Rabe J, van Kaick G. Can pre-operative contrast-enhanced dynamic MR imaging for prostate cancer predict microvessel density in prostatectomy specimens? Eur. Radiol. 2004; 14: 309–317.
25. Jager GJ, Ruijter ET, van de Kaa CA, de la Rosette JJ, Oosterhof GO, Thornbury JR, Ruijs SH, Barentsz JO. Dynamic TurboFLASH subtraction technique for contrast-enhanced MR imaging of the prostate: correlation with histopathologic results. Radiology 1997; 203: 645–652.
26. Preziosi P, Orlacchio A, Di Giambattista G, Di Renzi P, Bortolotti L, Fabiano A, Cruciani E, Pasqualetti P. Enhancement patterns of prostate cancer in dynamic MRI. Eur. Radiol. 2003; 13: 925–930.
27. Rouviere O, Raudrant A, Ecochard R, Colin-Pangaud C, Pasquiou C, Bouvier R, Maréchal JM, Lyonnet D. Characterization of time-enhancement curves of benign and malignant prostate tissue at dynamic MR imaging. Eur. Radiol. 2003; 13: 931–942.
28. Engelbrecht MR, Huisman HJ, Laheij RJ, Jager GJ, van Leenders GJ, Hulsbergen-Van De Kaa CA, de la Rosette JJ, Blickman JG, Barentsz JO. Discrimination of prostate cancer from normal peripheral zone and central gland tissue by using dynamic contrast-enhanced MR imaging. Radiology 2003; 229: 248–254.
29. McMahon CJ, Bloch BN, Lenkinski RE, Rofsky NM. Dynamic contrast-enhanced MR imaging in the evaluation of patients with prostate cancer. Magn. Reson. Imaging Clin. N. Am. 2009; 17: 363–383.
30. Bonekamp D, Macura KJ. Dynamic contrast-enhanced magnetic resonance imaging in the evaluation of the prostate. Top. Magn. Reson. Imaging 2008; 19; 273–284.
31. Macura KJ. Multiparametric magnetic resonance imaging of the prostate: current status in prostate cancer detection, localization, and staging. Semin. Roentgenol. 2008; 43: 303–313.
32. Futterer JJ, Heijmink SW, Scheenen TW, Veltman J, Huisman HJ, Vos P, Hulsbergen-Van de Kaa CA, Witjes JA, Krabbe PF, Heerschap A, Barentsz JO. Prostate cancer localization with dynamic contrast-enhanced MR imaging and proton MR spectroscopic imaging. Radiology 2006; 241: 449–458.
33. Ocak I, Bernardo M, Metzger G, Barrett T, Pinto P, Albert PS, Choyke PL. Dynamic contrast-enhanced MRI of prostate cancer at 3 T: a study of pharmacokinetic parameters. Am. J. Roentgenol. 2007; 189: 849.
34. Kim JK, Hong SS, Choi YJ, Park SH, Ahn H, Kim CS, Cho KS. Wash-in rate on the basis of dynamic contrast-enhanced MRI: usefulness for prostate cancer detection and localization. J. Magn. Reson. Imaging 2005; 22: 639–646.
35. Kim CK, Park BK, Kim B. Localization of prostate cancer using 3 T MRI – comparison of T2-weighted and dynamic contrast-enhanced imaging. J. Comput. Assist. Tomogr. 2006; 30: 7–11.
36. Engelbrecht MR, Huisman HJ, Laheij RJ, Jager GJ, van Leenders GJ, Hulsbergen-Van De Kaa CA, de la Rosette JJ, Blickman JG, Barentsz JO. Discrimination of prostate cancer from normal peripheral zone and central gland tissue by using dynamic contrast-enhanced MR imaging. Radiology 2003; 229: 248–254.
37. Ren J, Huan Y, Wang H, Chang YJ, Zhao HT, Ge YL, Liu Y, Yang Y. Dynamic contrast-enhanced MRI of benign prostatic hyperplasia and prostatic carcinoma: correlation with angiogenesis. Clin. Radiol. 2008; 63: 153–159.
38. Padhani AR, Gapinski CJ, Macvicar DA, Parker GJ, Suckling J, Revell PB, Leach MO, Dearnaley DP, Husband JE. Dynamic contrast enhanced MRI of prostate cancer: correlation with morphology and tumour stage, histological grade and PSA. Clin. Radiol. 2000; 55: 99–109.
39. Thomas MA, Narayan P, Kurhanewicz J, Jajodia P, Weiner MW. 1HMR spectroscopy of normal and malignant human prostates in vivo. J. Magn. Reson. 1990; 87: 610–619.
40. Kurhanewicz J, Vigneron DB, Nelson SJ, Hricak H, MacDonald JM, Konety B, Narayan P. Citrate as an in vivo marker to discriminate prostate cancer from benign prostatic hyperplasia and normal prostate peripheral zone: detection via localized proton spectroscopy. Urology 1995; 3: 459–466.
41. Govindaraju V, Young K, Maudsley AA. Proton NMR chemical shifts and coupling constants for brain metabolites. NMR Biomed. 2000; 13(3): 129–153.
42. Nagarajan R, Margolis D, Raman S, Sarma MK, Sheng K, King CR, Verma G, Sayre J, Reiter RE, Thomas MA. MR spectroscopic imaging and diffusion-weighted imaging of prostate cancer with Gleason scores. J. Magn. Reson. Imaging 2012; 36(3): 697–703.
43. Petroff OA, Rothman DL, Behar KL, Mattson RH. Initial observations on effect of vigabatrin on in vivo 1H spectroscopic measurements of gamma-aminobutyric acid, glutamate, and glutamine in human brain. Epilepsia 1995; 36(5): 457–464.
44. Trabesinger AH, Meier D, Boesiger P. In vivo 1H NMR spectroscopy of individual human brain metabolites at moderate field strengths. Magn. Reson. Imaging 2003; 21: 1295–1302.
45. Keltner JR, Wald LL, Christensen JD, Maas LC, Moore CM, Cohen BM, Renshaw PF. A technique for detecting GABA in the human brain with

PRESS localization and optimized refocusing spectral editing radiofrequency pulses. Magn. Reson. Med. 1996; 36: 458–461.
46. Rothman DI, Petroff OA, Behar KL, Mattson RH. Localized 1H NMR measurements of γ-aminobutyric acid in human brain in vivo. Proc. Natl Acad. Sci. USA 1993; 90: 5662–5666.
47. Lee HK, Yaman A, Nalcioglu O. Homonuclear J-refocused spectral editing technique for quantification of glutamine and glutamate by 1H NMR spectroscopy. Magn. Reson. Med. 1995; 34: 253–259.
48. Aue WP, Bartholdi E, Ernst RR. Two-dimensional spectroscopy – application to nuclear magnetic resonance. J. Chem. Phys. 1976; 64(5): 2229–2246.
49. Ryner LN, Sorenson JA, Thomas MA. 3-D localized 2D-NMR spectroscopy on an MRI scanner. J. Magn. Reson. B 1995; 107: 126–137.
50. Ryner LN, Sorenson JA, Thomas MA. Localized 2D J-resolved H-1 MR spectroscopy: strong coupling effects *in vitro and in vivo*. Magn. Reson. Imaging 1995; 13: 853–869.
51. Kreis R, Boesch C. Spatially localized, one- and two-dimensional NMR spectroscopy and in vivo application to human muscle. J. Magn. Reson. 1996; B113: 103–118.
52. Thomas MA, Yue K, Binesh N, Davanzo P, Kumar A, Siegel B, Frye M, Curran J, Lufkin R, Martin P, Guze B. Localized two dimensional shift correlated MR spectroscopy of human brain. Magn. Reson. Med. 2001; 46: 58–67.
53. Swanson MG, Vigneron DB, Tran TK, Sailasuta N, Hurd RE, Kurhanewicz J. Single-voxel oversampled J-resolved spectroscopy of in vivo human prostate tissue. Magn. Reson. Med. 2001; 45(6): 973–980.
54. Yue K, Marumoto A, Binesh N, Thomas MA. 2D JPRESS of human prostates using an endorectal receiver coil. Magn. Reson. Med. 2002; 47(6): 1059–1064.
55. Thomas MA, Binesh N, Yue K, Banakar S, Wyckoff N, Huda A, Marumoto A, Raman S. Adding a new spectral dimension to localized ^{1}H MR spectroscopy of human prostates using an endorectal coil. Spectroscopy 2003; 17(2/3): 521–527.
56. Nagarajan R, Gomez AM, Raman SS, Margolis DJ, McClure T, Thomas MA. Correlation of endorectal 2D JPRESS findings with pathological Gleason scores in prostate cancer patients. NMR Biomed. 2010; 23 (3): 257–261.
57. Ernst RR, Bodenhausen G, Wokaun A. *Principles of NMR Spectroscopy in One and Two Dimensions*. Oxford University Press: Oxford; 1987, pp. 283–533.
58. Levitt MH. *Spin Dynamics: Basics of Nuclear Magnetic Resonance*. Wiley: Chichester, UK; 2002, pp. 361–383.
59. Keeler J. *Understanding NMR Spectroscopy*. Wiley: Cambridge; 2002.
60. Ziegler A, Izquierdo M, Remy C, Decorps M. Optimization of homonuclear two-dimensional correlation methods for in vivo and ex vivo NMR. J. Magn. Reson. 1995; B107: 10–18.
61. Kumar A. Two-dimensional spin-echo NMR spectroscopy: a general method for calculation of spectra. J. Magn. Reson. 1978; 30: 227–249.
62. Delikatny EJ, Hull WE, Mountford CE. The effect of altering time domains and window functions in two-dimensional proton COSY spectra of biological specimens. J. Magn. Reson. 1991; 94: 563–573.
63. Thrippleton MJ, Edden RAE, Keeler J. Suppression of strong coupling artefacts in J-spectra. J. Magn. Reson. 2005; 174: 97–109.
64. Smith SA, Levante TO, Meier BH, Ernst RR. Computer simulations in magnetic resonance. An object-oriented programming approach. J. Magn. Reson. 1994; 106A: 75–105.
65. Cheng LL, Wu C, Smith MR, Gonzalez RG. Non-destructive quantitation of spermine in human prostate tissue samples using HRMAS 1H NMR spectroscopy at 9.4 T. FEBS Lett. 2001; 494: 112–116.
66. Serkova NJ, Gamito EJ, Jones RH, O'Donnell C, Brown JL, Green S, Sullivan H, Hedlund T, Crawford ED. The metabolites citrate, myo-inositol, and spermine are potential age-independent markers of prostate cancer in human expressed prostatic secretions. Prostate 2008; 68: 620–628.
67. Van der Graaf M, Schipper RG, Oosterhof GO, Schalken JA, Verhofstad AA, Heerschap A. Proton MR spectroscopy of prostatic tissue focused on the detection of spermine, a possible biomarker of malignant behavior in prostate cancer. Magn. Reson. Mater. Phys. Biol. Med. 2000; 10: 153–159.
68. Mi Z, Kramer DL, Miller JT, Bergeron RJ, Bernacki R, Porter CW. Human prostatic carcinoma cell lines display altered regulation of polyamine transport in response to polyamine analogs and inhibitors. Prostate 1998; 34: 51–60.
69. Lange T, Schulte RF, Boesiger P. Quantitative J-resolved prostate spectroscopy using two-dimensional prior-knowledge fitting. Magn. Reson. Med. 2008; 59(5): 966–972.
70. Baker EH, Basso G, Barker PB, Smith MA, Bonekamp D, Horská A. Regional apparent metabolite concentrations in young adult brain measured by (1)H MR spectroscopy at 3 Tesla. J. Magn. Reson. Imaging 2008; 27(3): 489–499.
71. Mlyanarik V, Gruber S, Moser E. Proton T(1) and T(2) relaxation times of human brain metabolites at 3 Tesla. NMR Biomed. 2001; 5: 325–331.
72. Schulte RF, Lange T, Beck J, Meier D, Boesiger P. Improved two-dimensional J-resolved spectroscopy. NMR Biomed. 2006; 19: 264–270.
73. Mansfield P. Spatial mapping of the chemical shift in NMR. Magn. Reson. Med. 1984; 1: 370–386.
74. Matsui S, Sekihara K, Kohno H. High speed spatially resolved NMR spectroscopy using phase modulated spin echo trains. Expansion of the spectral bandwidth by combined use of delayed spin echo trains. J. Magn. Reson. 1985; 64: 167–171.
75. Posse S, Tedeschi G, Risinger R, Ogg R, Bihan DL. High speed 1H spectroscopic imaging in human brain by echo planar spatial-spectral encoding. Magn. Reson. Med. 1995; 33: 34–40.
76. Ebel A, Soher BJ, Maudsley AA. Assessment of 3D proton MR echo-planar spectroscopic imaging using automated spectral analysis. Magn. Reson. Med. 2001; 46: 1072–1078.
77. Mulkern RV, Panych LP. Echo planar spectroscopic imaging. Concepts Magn. Reson. 2001; 13: 213–237.
78. Du W, Du YP, Fan X, Zamora MA, Karczmar GS. Reduction of spectral ghost artifacts in high-resolution echo-planar spectroscopic imaging of water and fat resonances. Magn. Reson. Med. 2003; 49(6): 1113–1120.
79. Chen AP, Cunningham CH, Ozturk-Isik E, Xu D, Hurd RE, Kelley DA, Pauly JM, Kurhanewicz J, Nelson SJ, Vigneron DB. High speed 3 T MR spectroscopic imaging of prostate with flyback echo-planar encoding. J. Magn. Reson. Imaging 2007; 25: 1288–1292.
80. Du W, Fan X, Foxley S, Zamora M, River JN, Culp RM, Karczmar GS. Comparison of high resolution echo-planar spectroscopic imaging with conventional MR imaging of prostate tumors in mice. NMR Biomed. 2005; 18: 285–292.
81. Lipnick S, Verma G, Ramadan S, Furuyama J, Thomas MA. Echo planar correlated spectroscopic imaging: implementation and pilot evaluation in human calf in vivo. Magn. Reson. Med. 2010; 64: 947–956.
82. Nagarajan R, Furuyama J, Margolis D, Raman S, Sarma M, Thomas M. Echo planar based J resolved and correlated spectroscopic imaging of human prostate using external coil. In: *Proceedings of the ISMRM, Montreal, Canada, 2011*. p. 2801.
83. Hennig J, Nauerth A, Friedburg H. RARE imaging: a fast imaging method for clinical MR. Magn. Reson. Med. 1986; 3: 823–833.
84. Constable R, Smith R, Gore J. Signal-to-noise and contrast in fast spin echo (FSE) and inversion recovery FSE imaging. J. Comput. Assist. Tomogr. 1992; 16(1): 41–47.
85. Listerud J, Einstein S, Outwater E, Kressel HY. First principles of fast spin echo. Magn. Reson. Q. 1992; 8(4): 199–244.
86. Duyn JH, Moonen CTW. Fast proton spectroscopic imaging of human brain using multiple spin-echoes. Magn. Reson. Med. 1993; 30: 409–414.
87. Dydak U, Meier D, Lamerichs R, Boesiger P. Trading spectral separation at 3 T for acquisition speed in multi spin-echo spectroscopic imaging. Am. J. Neruroradiol. 2006; 27: 1441–1446.
88. Rutgers DR, van der Grond J. Relaxation times of choline, creatine and N-acetyl aspartate in human cerebral white matter at 1.5 T. NMR Biomed. 2002; 3: 215–221.
89. Nagarajan R, Furuyama J, Sarma MK, Margolis D, Raman S, Reiter RE. Multi-echo EP-based J-resolved magnetic resonance spectroscopic imaging of prostate cancer. In: *RSNA–Scientific Meeting 2011 (Chicago, USA)*. Abstract 186.
90. Donoho D. Compressed sensing. IEEE Trans. Info. Theory 2006; 52: 1289–1306.
91. Candez EJ, Romberg J, Tao T. Stable signal recovery from incomplete and inaccurate measurements. Commun. Pure Appl. Math. 2006; 59: 1207–1221.
92. Lustig M, Donoho D, Pauly JM. Sparse MRI: the application of compressed sensing for rapid MR imaging. Magn. Reson. Med. 2007; 58 (6): 1182–1195.
93. Doneva M, Börnert P, Eggers H, Mertins A, Pauly J, Lustig M. Compressed sensing for chemical shift-based water–fat separation. Magn. Reson. Med. 2010; 64(6): 1749–1759.

94. Hu S, Lustig M, Chen AP, Crane J, Kerr A, Kelley DA, Hurd R, Kurhanewicz J, Nelson SJ, Pauly JM, Vigneron DB. Compressed sensing for resolution enhancement of hyperpolarized 13C flyback 3D-MRSI. J. Magn. Reson. 2008; 192(2): 258–264.
95. Gamper U, Boesiger P, Kozerke S. Compressed sensing in dynamic MRI. Magn. Reson. Med. 2008; 59: 365–373.
96. Michailovich O, Rathi Y, Dolui S. Spatially regularized compressed sensing for high angular resolution diffusion imaging. IEEE Trans. Med. Imaging 2011; 30: 1100–1115.
97. Wu B, Millane RP, Watts R, Bones PJ. Prior estimate based compressed sensing in parallel MRI. Magn. Reson. Med. 2011; 65: 83–95.
98. Hu S, Lustig M, Balakrishnan A, Larson PE, Bok R, Kurhanewicz J, Nelson SJ, Goga A, Pauly JM, Vigneron DB. 3D compressed sensing for highly accelerated hyperpolarized 13C MRSI with in vivo applications to transgenic mouse models of cancer. Magn. Reson. Med. 2010; 63: 312–321.
99. Scheenen TW, Heijmink SW, Roell SA, Hulsbergen-Van de Kaa CA, Knipscheer BC, Witjes JA, Barentsz JO, Heerschap A. Three-dimensional proton MR spectroscopy of human prostate at 3 T without endorectal coil: feasibility. Radiology 2007; 245: 507–516.
100. Kim DH, Margolis D, Xing L, Daniel B, Spielman D. In vivo prostate magnetic resonance spectroscopic imaging using two-dimensional J-resolved PRESS at 3 T. Magn. Reson. Med. 2005; 53(5): 1177–1182.
101. Goldstein T, Osher S. The split Bregman method for L1-regularized problems. SIAM Journal on Imaging Sciences 2009; 2(2): 323–343.
102. Furuyama J, Wilson N, Burns B, Nagarajan R, Margolis D, Thomas MA. Application of compressed sensing to multidimensional spectroscopic imaging in human prostate. Magn. Reson. Med. 2012; 67: 1499–1505.
103. DeFeo EM, Cheng LL. Characterizing human cancer metabolomics with *ex vivo* 1H HRMAS MRS. Technol. Cancer Res. Treat. 2010; 9: 381–391.
104. Stenman K, Stattin P, Stenlund H, Riklund K, Gröbner G, Bergh A. 1H HRMAS NMR derived biomarkers related tumor grade, tumor cell fraction, and cell proliferation in prostate tissue samples. Biomarker Insights 2011; 6: 39–47.
105. Swanson MG, Vigneron DB, Tabatabai ZL, Males RG, Schmitt L, Carroll PR, James JK, Hurd RE, Kurhanewicz J. Proton HR-MAS spectroscopy and quantitative pathologic analysis of MRI/3D-MRSI-targeted post-surgical prostate tissues. Magn. Reson. Med. 2003; 50: 944–954.
106. Wright A, Tessem MB, Bertilsson H, Grinde MT, Giskeødegård GF, Halgunset J, Angelsen A, Heerschap A, Gribbestad IS. Quantitative 1H HR-MAS using LC Model shows glutamate, choline, glycerylphosphocholine, and glucose as biomarkers of prostate. Proc. Intl Soc. Magn. Reson. Med. 2012; 20: 2975.
107. Thomas MA, Lange T, Velan SS, Nagarajan R, Raman S, Gomez A, Margolis D, Swart S, Raylman RR, Schulte RF, Boesiger P. Two-dimensional MR spectroscopy of healthy and cancerous prostates in vivo. Magn. Reson. Mater. Phys. Biol. Med. 2008; 21(6): 443–458.
108. Cavassila S, Deval S, Huegen C, van Ormondt D, Graveron-Demilly D. Cramer–Rao bound expressions for parametric estimation of overlapping peaks: influence of prior knowledge. J. Magn. Reson. 2000; 143(2): 311–320.
109. Sarma MK, Huda A, Nagarajan R, Hinkin CH, Wilson N, Gupta RK, Frias-Martinez E, Sayre J, Guze B, Han SH, Thomas MA. Multi-dimensional MR spectroscopy: towards a better understanding of hepatic encephalopathy. Metab. Brain Dis. 2011; 26(3): 173–184.
110. Nagarajan R, Sarma MK, Thames AD, Castellon SA, Hinkin CH, Thomas MA. 2D MR spectroscopy combined with prior-knowledge fitting is sensitive to HCV associated cerebral metabolic abnormalities. Int. J. Hepatol. 2012; 2012: 179365.